

General Disclaimer

One or more of the Following Statements may affect this Document

- This document has been reproduced from the best copy furnished by the organizational source. It is being released in the interest of making available as much information as possible.
- This document may contain data, which exceeds the sheet parameters. It was furnished in this condition by the organizational source and is the best copy available.
- This document may contain tone-on-tone or color graphs, charts and/or pictures, which have been reproduced in black and white.
- This document is paginated as submitted by the original source.
- Portions of this document are not fully legible due to the historical nature of some of the material. However, it is the best reproduction available from the original submission.

Analysis of Seismic Body Waves Excited by
the Mt. St. Helens Eruption of May 18, 1980

(NASA-CR-169741) ANALYSIS OF SEISMIC BODY N83-15968
WAVES EXCITED BY THE MOUNT SAINT HELENS
ERUPTION OF MAY 18, 1980 (California Inst.
of Tech.) 40 p HC A03/MF A01 CSCL 08K Unclas
G3/46 02399

Hiroo Kanamori, Jeffrey W. Given and Thorne Lay

Seismological Laboratory
California Institute of Technology
Pasadena, California 91125



Abstract

Seismic body waves which were excited by the May 18, 1980 eruption of Mt. St. Helens, and recorded by the Global Digital Seismographic Network (GDSN) stations are analyzed to determine the nature and the time sequence of the events associated with the eruption. The polarity of teleseismic P waves (period 20 sec) is identical at six stations which are distributed over a wide azimuthal range. This observation, together with a very small S to P amplitude ratio (at 20 sec), suggests that the source is a nearly vertical single force that represents the counter force of the eruption. The time history of the vertical force suggests two distinct groups of events, about two minutes apart, each consisting of several subevents with a duration of about 25 sec. The magnitude of the force is approximately 2.6×10^{17} dyne. This vertical force is in contrast with the long-period (~ 150 sec) southward horizontal single force which has been determined by a previous study and interpreted to be due to the massive landslide. The direction of the P-wave first motion observed at two nearby stations is consistent with the radiation pattern expected for the landslide, and suggests that a spontaneous landslide represents the beginning of the eruptive sequence, rather than the landslide having been triggered by a tectonic earthquake. The ground motions observed at station LON ($\Delta = 67$ km) are dominated by Rayleigh waves (i.e. Lamb pulse) and provide tight constraints on the time sequence of the events.

1. Introduction

Kanamori and Given (1982) analyzed long-period (~ 200 sec) surface waves excited by the eruption of Mt. St. Helens on May 18, 1980, and concluded that the source can be adequately represented by a nearly horizontal single force pointed in a direction $S5^{\circ}W$ having a characteristic time constant of about 150 sec. They interpreted this single force as due to the massive landslide (total volume $\approx 2.5 \text{ km}^3$) on the north slope of Mt. St. Helens (see Voight *et al.*, 1982). They also analyzed relatively short-period (~ 20 sec) body waves at teleseismic distances and interpreted them in terms of sequences of short-period events during the first several minutes of the eruption. However, because of the very complex and emergent character of the body-wave form, detailed analysis could not be made.

While the paper by Kanamori and Given was in press, we were informed by Dr. Robert Engdahl of the U. S. Geological Survey that a digital recording system was in operation at the WWSSN station at Longmire (LON; $\Delta = 67$ km and azimuth = 26° from the summit of Mt. St. Helens) and recorded seismic waves excited by the eruption. On our request, three-component long and intermediate period seismograms and a vertical component short-period seismogram from station LON were made available to us by the U.S. Geological Survey. These records provided us with key information regarding the timing of the events, and motivated us to perform further analyses of body waves recorded by the Global Digital Seismographic Network (GDSN).

This paper, which is a follow-up of Kanamori and Given (1982) reports our findings concerning relatively short-period events

associated with the eruption of Mt. St. Helens.

2. Data and Analysis

2.1 Far-Field Data

Figure 1 summarizes the body-wave signals recorded by 7 GDSN stations. The P waves are recorded at 6 stations with relatively good azimuthal coverage. The traces are lined up with respect to the Jeffreys-Bullen P arrival times calculated for the origin time of the $M_s = 5.2$ ($m_b = 4.7$) event (NEIS, O.T. $15^{\text{h}}32^{\text{m}}11^{\text{s}}$ GMT, May 18, 1980; 46.214°N , 122.194°W). The asterisks (*) indicate the ASRO (Abbreviated Seismological Research Observatory) stations; all others are SRO stations. The group delay time of the ASRO instruments is 4 sec longer than that of the SRO instruments at a period of 20 sec, which is the dominant period of the observed P waves. Therefore, the traces of the ASRO stations (KON, ZOB, and MAT) should be displaced to the left by 4 sec to be compared with those of the SRO stations (GRF, BOC, and GUM). Allowing for this, we observe that the waveforms at all stations during the first 3 min after the P time have the same polarity.

The S waves shown in Figure 1 are the transverse component and are plotted in a manner similar to the P waves. We find that the polarity of the waveforms observed at the stations to the east of the source (i.e., KON, GRF, BOC, and ZOB) is reversed with respect to that to the west (i.e., MAJ and TAT). Other important features are that the amplitudes of the P waves are about the same as those of the S waves, and the dominant period of the S waves is about 35 sec, which is significantly longer than the 25 sec dominant period of the P waves (see Figure 4a). The maximum amplitude and the polarity of the P and S waves

are plotted in Figure 2 as a function of azimuth. In this plot, the ASRO instrument responses are equalized to the SRO response and a small correction is made for geometrical spreading to normalize the amplitudes to $\Delta = 76^\circ$, the distance to GRF. The amplitude variation due to the difference in take-off angle is ignored.

Since the number of stations is very small, we cannot interpret this data set unambiguously in terms of the source force system. However, it is difficult to explain the P to S amplitude ratio by using a standard double couple source. Any double couple source would yield S waves with amplitudes several times larger than those of the P waves.

In view of the result of Kanamori and Given (1982) obtained from long-period surface waves, it is reasonable to try to explain this radiation pattern using a single force. Referring to the spherical coordinate system shown in Figure 3, the displacement field at (r, θ, ϕ) in a homogeneous elastic whole space (density: ρ , P velocity: α , S velocity: β) due to a single force $h(t)$ (t = time) applied at the origin on x-z plane is given by:

$$\begin{pmatrix} U_r \\ U_\theta \\ U_\phi \end{pmatrix} = \frac{1}{4\pi\rho r \alpha^2} h \left(t - \frac{r}{\alpha} \right) \begin{pmatrix} \sin\theta \cos\delta \cos\phi - \cos\theta \sin\delta \\ 0 \\ 0 \end{pmatrix} + \frac{1}{4\pi\rho r} \frac{1}{\beta^2} h \left(t - \frac{r}{\beta} \right) \begin{pmatrix} 0 \\ \cos\delta \cos\theta \cos\phi + \sin\delta \sin\theta \\ -\sin\phi \cos\delta \end{pmatrix} \quad (1)$$

where δ is the dip angle of the force measured from the horizontal. If the take-off angle of the ray is i_h , and the azimuth of the station and the force measured clockwise from the north are ϕ_s and ϕ_f respectively, then $i_h = \pi - \theta$, and $\phi = \phi_f - \phi_s$.

If we assume the same geometry of the force as that determined from the surface waves, i.e., $\phi_f = 185^\circ$, $\delta = 0^\circ$, the radiation pattern becomes two-lobed for both P and S waves as shown by the curves labeled $\delta = 0^\circ$ in Figure 2. These curves are calculated with $i_h = 20^\circ$ which corresponds to $\Delta = 76^\circ$. Since the take-off angle varies from station to station, we need to apply a small correction to the data to compare them with the computed curve. However, this correction is very small, $\pm 13\%$ at most, and is not applied here. It is clear from Figure 2 that the horizontal single force cannot explain the constant polarity of the P waves and the amplitude ratio of P to S waves. The magnitude of the force, f , assigned to each curve in Figure 2 is determined by using a synthetic seismogram computed for a symmetric triangular source time function having a width of 25 sec. The method is described later.

In order to explain the amplitude ratio, the dip angle, δ , should be increased as shown in Figure 2; $\delta = 60^\circ$ gives an approximately correct S to P ratio as well as a constant P-wave polarity. However, this geometry is not satisfactory because, as mentioned earlier, the period of the S waves is much longer than that of the P waves (see Figure 4a). The difference in Q between P and S waves cannot explain this difference in period. Figure 4b compares the waveforms of synthetic P and S waves computed for a symmetric triangular source function having a width, t_w^* , of 20 sec. For this computation, t_α^* and t_β^*

(travel time divided by Q averaged over the path) are assumed to be 1 and 4 sec, respectively, the values commonly used in teleseismic body-wave studies. The difference in period between the synthetic P and S waves is much smaller than that observed.

Figure 4b also shows a synthetic S wave for a triangular source function with $t_w = 35$ sec. A triangular function with $t_w = 20$ sec can explain the dominant period of the P wave, while a width of 35 sec is required to explain the period of the S wave. If we consider the spectral component of the S waves that has approximately the same period as the P waves, the S to P amplitude ratio would be even smaller than that indicated by Figure 2. In other words, as far as short-period ($T < 25$ sec) waves are concerned, the S waves are essentially at the noise level, and all the stations are nodal. This observation, together with the constant amplitude and the uniform polarity of the P waves, suggests that the dip angle of the force is significantly larger than 60° . In the following discussion, we use a vertical ($\delta = 90^\circ$) force for simplicity, but the actual dip angle can be in a range from 80° to 90° .

The source of the S waves remains to be explained. The observed polarity reversal between the groups of the stations to the east and to the west of the source is consistent with the polarity reversal of long-period Love waves (Kanamori and Given, 1982). This suggests that both the S and Love waves are produced by the same source, a horizontal single force directed in $S5^\circ W$. In order to investigate this possibility, we band-pass filter the SH waves using a filter described in Kanamori and Stewart (1979) with cut-off periods of 65 and 1,000 sec. Figure 5 shows the filtered seismograms, and the maximum amplitudes are

plotted in Figure 6 after the difference in geometric spreading factor is corrected. The amplitudes are corrected to a distance of 76°.

In Figure 5, the arrival time of SS is indicated by a dot. Since we are primarily interested in the direct S phase, we indicate by a dotted curve the portion of the filtered records which may be contaminated by the SS phase.

Figures 5 and 6 clearly indicate the polarity reversal between the eastern and the western stations and the nodal character of stations KON and GRF. We compute synthetic seismograms for a single force with the source time history

$$f(t) = \begin{cases} (1/2) (1 - \cos (\frac{t}{\tau} \pi)) & 0 \leq t \leq 2\tau \\ 0 & t \geq 2\tau \end{cases} \quad (2)$$

determined by Kanamori and Given (1982). We assume a homogeneous half-space and use the method described in Kanamori and Stewart (1976) with the double couple source replaced by the single force source given by (1). Seismic rays corresponding to S and sS are included, and the same filter as that used for the data is applied. Figure 7 compares the synthetics with the observed (filtered) seismograms. The amplitude of synthetic seismograms computed for $f_0 = 1 \times 10^{18}$ dyne, the magnitude of the force determined from long-period surface waves, is plotted as a function of azimuth in Figure 6. Although the synthetic waveforms are similar to the observed, the predicted amplitudes are considerably larger than observed. This discrepancy may be due to the difference in the period of the SH waves (about 100 sec) shown in Figure 5 and the surface waves (about 200 sec) used for the determination of the

magnitude of the force. It is possible that the shape of the time function (2) is not very accurate and the amplitude of the short-period component is about 70% smaller than that given by (2), or the geometry of the source at short periods is slightly different from that at long periods. Despite this difference, the approximate agreement in amplitude and polarity indicates that the observed long-period SH waves are produced by the same source as that for the long-period surface waves. For the same reason, we believe that the SH waves with a period of about 35 sec shown in Figure 1 are due to somewhat irregular components of the horizontal single force.

We next determine the time history of the vertical single force by removing the instrument response from the observed P-wave seismograms. Because of the very narrow frequency band of the SRO and the ASRO seismographs, unambiguous determination of the source time history is difficult. Since the waveforms of the observed P waves are essentially identical at all the stations, we take the GRF record and deconvolve it with the instrument response over a relatively narrow period band, 8 to 100 sec. The deconvolved signal is reshaped by a series of triangular functions as shown in Figure 8e. Then this time function is used to compute the synthetic seismogram for station GRF. For this computation, a vertical (downward) single force is applied at the surface of a homogeneous half-space and contributions from P, pP, and sP phases are added. The synthetic seismogram for GRF is shown in Figure 8b with the observed waveform. The same time history is also used in the synthetic for station MAJ (Figure 8d) which is also compared with the observed (Figure 8c). The overall agreement between the observed and the

synthetic waveforms is satisfactory. We note, however, that because of the narrow-band response of the instrument, the long-period trend cannot be determined, which causes some ambiguity in the polarity of the triangular pulses. For example, it is possible to explain the observed waveforms equally well by a series of negative pulses. The seismogram at MAJ has fairly large background noise, and the direction of the first motion is difficult to determine. The first motion of the GRF record is more distinct. If we take the upward motion at about 8 sec after the JB time as the first motion, the polarity of the first triangular pulse should be positive. (Note the delay of the onset of the synthetic seismogram with respect to the onset of the triangular source function. This delay is due to the large group delay time of the SRO and ASRO seismographs.)

Although the details of the source functions cannot be resolved, the triangular source function shown in Figure 8e clearly indicates two distinct groups of events about 2 minutes apart, each consisting of several subevents. Between the two events, there is a period of quiescence for about 30 seconds. This character is readily apparent in the original P-wave data as seen in Figure 1.

By matching the amplitude of the synthetic and the observed seismograms, we determine the peak value of the single force to be 2.8×10^{17} dyne and 2.4×10^{17} dyne for GRF and MAJ, respectively, as shown in Figure 8. The average for all the stations is 2.6×10^{17} dyne (see also Figure 2).

A similar analysis is made to determine the magnitude of the force responsible for the short-period (~ 35 sec) component of the S wave.

Since the waveform varies from station to station (see Figure 1) after the first cycle, here we attempt to estimate the magnitude of the single force responsible for the first cycle. We find that a symmetric triangular source function having a width of 35 sec can explain the observed period of the S waves. The magnitude of the force is 0.7 to 1.4×10^{17} dyne, if a horizontal single force is assumed. This value is almost an order of magnitude smaller than that of the long-period component determined from surface waves and long-period S waves. Thus, the short-period component represents a very minor perturbation to the time history given by (2).

2.2 Near-Field Data

At station Longmire (LON), digital long-period, intermediate-period, and short-period seismograms were obtained. The long-period (DWWSSN LP) records went off-scale about 20 sec after the first arrival, but they clearly indicate a downward first motion (Figure 9). The first motion on the short-period seismogram (DWWSSN SP) is also downward, although it is less clear than the other records (Figure 9). The onset time of the first motion is about 11 sec after the origin time of the $M_b = 5.2$ earthquake. Since this delay is approximately equal to the travel time of P waves from the summit of Mt. St. Helens, we consider that this first motion represents the P arrival of the $M_b = 5.2$ earthquake, the very beginning of the eruption sequence (Voight et al., 1982).

Weaver et al. (1982) report that the events which occurred to the southeast of the summit had right-lateral strike-slip mechanisms on a fault striking in $N15^{\circ}W$. This mechanism would place LON in the

dilatational quadrant. Thus, the observed downward initial motion may indicate that the $M_s = 5.2$ event was a tectonic earthquake with this mechanism. However, the first-motion at the WWSSN station at Corvalis which is almost opposite to LON in azimuth (COR, $\Delta = 1.79^\circ$, Azimuth = 206°) does not support this idea. For the distance of 1.79° (199 km) to COR, the P-wave travel time would be approximately 30 sec and the first-motion from the $M_s = 5.2$ event would arrive at COR at $15^{\text{h}}32^{\text{m}}41^{\text{s}}$. As Figure 9 shows, the direction of the first-motion at COR at this time is up, which is inconsistent with the strike-slip mechanism. One possible explanation is that the $M_s = 5.2$ earthquake represents the beginning of the landslide itself. Since the equivalent force system for the landslide is the nearly horizontal southward single force, the first motion would be down at LON and up at COR. Since no other long-period data are available, we cannot determine the mechanism unambiguously. However, these first-motion data and the very quiet trace before the onset at LON (particularly for the SP trace) are suggestive of a process in which the landslide triggered the entire eruption sequence rather than the landslide having been triggered by a tectonic earthquake.

Since the intermediate-period records are most complete, we make a more detailed examination of these records. First, we deconvolve the instrument response over a pass-band from 1.8 to 150 sec with the result shown in Figure 10b. The long-period oscillation is caused by the cut-off at the long-period end, and is spurious. The relatively short-period oscillations superposed on the long-period trend represent the real signal. Figure 10c is obtained by convolving the WWSSN

long-period response with the deconvolved trace, and is equivalent to the standard WWSSN LP seismogram.

We next convolve the deconvolved trace (Figure 10b) with the ~~SAC~~ response to compare it with the far-field waveforms shown in Figure 1 (Figure 11a). A striking similarity between this trace and any one of the far-field records (e.g., GRF, see Figure 11b) is found during the first 4 minutes. Figures 11a and 11b are matched up at the P wave arrival time. However, a closer inspection reveals that if we flip the polarity of Figure 11a and shift it backward by about 9 sec, the waveform similarity is even more striking (see Figure 11c). This shift of 9 sec in time is equivalent to matching the P-wave arrival time at GRF with the arrival time of a wave with a velocity of 3.1 km/sec at LON (see Figures 11b and 11c). This result can be explained by using the solution of the classic Lamb's problem (Lamb, 1904). That is, the LON record essentially represents the Rayleigh wave due to the vertical single force applied at the source. For a step-function single force applied vertically downward at the free surface of a homogeneous elastic half-space (rigidity = μ), the displacement at distance r on the free surface is given essentially by a step function with the amplitude of $0.37/\pi\mu r$ (downward) propagating with the Rayleigh-wave velocity with a delta-function like singularity preceding it (e.g., see Richards, 1979, figure 2c). When this response is convolved with the instrument response, the delta-function pulse has only negligible contribution so that the overall response is given by the step function propagating with the Rayleigh velocity. For a downward vertical force, the main P-wave pulse at GRF is upward while the main Rayleigh-wave pulse at LON is

downward. Thus, the LON record should be reversed in polarity and shifted in time by the amount equal to the difference in the P-wave and Rayleigh-wave travel times to be matched against the GRF record.

Since the waveform of Rayleigh waves at a short distance directly represents the time history of the force at the source, we can use the deconvolved trace at LON to check the result we obtained from the far-field data. As Figure 10 shows, the deconvolved trace indicates a series of pulses, each having a duration of 20 to 30 sec. However, because of the lack of response at long-periods, the base line cannot be determined unambiguously. Here we consider two extreme cases. First, we use the upper envelope shown by a dotted curve in Figure 10b as the base line. In this case, the displacement is a series of downward pulses as shown by S_1 in Figure 10d. The seven subevents represented by the pulses are indicated by E_i ($i = 1, 2, \dots, 7$). This time series can be interpreted as a sequence of downward vertical forces. Subevent E_1 starts at, or a few seconds after, the arrival of the Rayleigh wave (indicated by t_R). This event contains a large amount of short-period energy as shown in Figure 10a, and E_1 is followed by two large long-period (~20 sec) pulses, the first one beginning at about 22 sec after t_R . The first sequence of subevents, $E_1-E_2-E_3-E_4$, ends at about 1 min 40 sec after t_R , and is followed by a quiet period lasting for about 35 sec. The second sequence which consists of three subevents, $E_5-E_6-E_7$, starts at 2 min 15 sec after t_R . Another notable feature is that during the period between E_4 and E_5 when the long-period record indicates quiescence, the amplitude on the short-period record is relatively large.

For the second extreme case, we use the lower envelope indicated by a dot-dash curve in Figure 10b as the base line. In this case, the event sequence S_2 (Figure 10e) is obtained. Although the overall structure (two events 2 min apart) is similar to that of S_1 , the polarity of the forces is opposite to that of S_1 .

These two event sequences, S_1 and S_2 , are convolved with the WWSSN instrument response and are compared with the observed trace in Figure 12. Both sequences can explain the overall feature of the observed record satisfactorily. Assuming that the observed signal represents the Rayleigh wave excited by a vertical single force, we can determine the magnitude of the force. Assuming a homogeneous half-space with a rigidity $\mu = 2.0 \times 10^{11}$ dyne/cm², we obtain 3.1×10^{17} dyne for the peak value of S_1 and S_2 . This value is about 20% larger than that obtained from the far-field data, but is considered reasonable in view of the very simple half-space model used here. Since the far-field value is determined by the records from many stations, we consider it more reliable and will use it hereafter. However, the LON record probably represents the source time history more accurately than the far-field records.

The actual event sequence is probably somewhere between these two extreme cases. However, the relatively abrupt downward motion at about 2 sec after t_R both on the short- and long-period records indicates that the first triangular pulse is probably downward and the sequence given by S_1 is preferable. The polarity of the later subevents is more difficult to determine. We will use S_1 for the discussion below, but the uncertainty in the overall polarity should be borne in mind. The

event sequence S_1 is similar to the one determined from teleseismic data shown in Figure 8, although they differ in details.

On the basis of these results, we conclude that two major events occurred approximately 2 minutes apart during the first 4 minutes. Each event has several subevents. The first event occurred within a few seconds after t_R and contains a relatively large amount of high-frequency energy. Since t_R corresponds to the Rayleigh-wave travel time from the $M_s = 5.2$ event, the beginning of the first event is considered to be within a few seconds after this earthquake.

3. Discussion

The time histories of the vertical force determined from the far-field and near-field data are shown in Figure 13 together with that of the long-period horizontal single force determined by Kanamori and Given (1982). Some results from various on-site observations are also included.

Although the time sequence of the forces determined here can be used as a relatively objective constraint for various models of the eruption sequence, its interpretation is not unique. Here, we attempt to provide one possible interpretation on the basis of the various seismological observations reported in this paper. Since the interpretation of the long-period signals in terms of the landslide is discussed in detail in Kanamori and Given (1982), here we focus on the short-period events.

According to the descriptions and reconstructions of the eruption sequence by various investigators (Voight et al., 1982; Moore and Albee, 1982; Malone et al., 1982), the sequence during the first several

minutes can be generally described as follows.

The eruption on May 18, 1980 began as a large seismic event. Within 7 to no more than 20 sec after this event, the north slope began to slide northward. As the slide developed and progressed, steam and magmatic explosions began due to pressure release behind the slide scarp, and the slide became engulfed in the resulting blast cloud. A second large earthquake occurred about 2 minutes after the first.

Although we could not determine the mechanism of the initial $M_s = 5.2$ event unambiguously, the first-motion data at YON and COR suggest that this earthquake may represent the beginning of the landslide. The first event E_1 (see also Figure 10) which contains a relatively large amount of high-frequency energy may represent the initial stage of the eruption before the vent had been fully uncapped. Events E_2 , E_3 , and E_4 can be interpreted as due to the explosions that were triggered by removal of the overburden pressure. The relatively quiet period after E_4 may represent the end of the initial series of explosions; the significance of the increased amplitude of the short-period waves shown in Figure 10a during this quiet period is not clear. Events E_5 , E_6 , and E_7 appear to represent the second sequence of explosions described by Moore and Rice (1982). Moore and Rice report, on the basis of measurements from infrared sensors aboard two U. S. Air Force satellites and of ground photographic and eyewitness records, that a second explosion occurred a few km north of the first, about 1.5 minutes later. Moore and Rice (1982) conclude that this second explosion was the largest of the eruptions and caused most of the damage and tree blowdown.

The magnitude of the force, about 2.6×10^{17} dyne, is comparable to the value, 3.3×10^{17} dyne, estimated by Kieffer (1981, 1982) using a steady-flow model for a multiphase (vapor-solid-liquid) mixture expanding from the vent. However, the orientation of the force determined from the seismic data is nearly vertical, while the model used by Kieffer (1981) is for a lateral blast. The short-period S wave data (Figure 1) indicate some horizontal component ($\sim 1 \times 10^{17}$ dyne), but it can be due to either the irregular motion of the landslide or the horizontal component of the force due to the blast. As discussed in Kanamori and Given (1982), the horizontal force is dominated by a very long-period component.

It should also be noted that a part of the seismic excitation could be due to some processes that occurred within the magma chamber and may not be directly related to the surface eruption.

4. Conclusion

The radiation pattern of P and S waves (period 20 to 30 sec) excited by the May 18, 1980, Mt. St. Helens eruption and their amplitude ratio can be explained by a nearly vertical single force at the source with a magnitude of about 2.6×10^{17} dyne. The time history of this vertical force suggests two distinct groups of events each consisting of several subevents, with a duration of about 25 sec. The two groups are separated in time by approximately 2 minutes. This vertical force is in contrast with the long-period (duration > 150 sec) horizontal single force with a magnitude of 10^{18} dyne determined by Kanamori and Given (1982). We interpret that this vertical force represents the counter-force of the eruption.

Although the direction of the first motion is ambiguous at teleseismic stations, it is clearly recorded at two stations at short distances, LON and COR. The first motion is up at COR ($\Delta = 199$ km, $\phi = 206^\circ$) and down at LON ($\Delta = 68$ km, $\phi = 26^\circ$) which is opposite in azimuth to COR. This pattern of the first motion is consistent with that expected for the southward horizontal single force, and suggests, though not definitely, that the landslide represents the very beginning of this entire eruptive sequence. If this interpretation is correct, gravitational instability caused by the pre-eruption bulging of the north slope near the summit of Mt. St. Helens resulted in spontaneous outbreak of the massive landslide. The beginning of the $M_s = 5.2$ earthquake at $15^{\text{h}}32^{\text{m}}11^{\text{s}}$ GMT probably represents the landslide itself rather than a tectonic event that triggered the landslide.

The ground motion observed at LON can be interpreted as Rayleigh waves excited by the vertical single force associated with the eruption, and is considered a Lamb pulse in nature. The waveform of this Lamb pulse provides constraints on the time sequence of the events during the first 3 min after the beginning of the eruption, and on the magnitude of the force.

Acknowledgment

We thank Robert Engdahl and John Hoffman of the U. S. Geological Survey for making available to us the digital seismograms used in this study. This research was partially supported by National Aeronautics and Space Administration grant Number NSG-7610. Contribution No. 3854, Division of Geological and Planetary Sciences, California Institute of Technology, Pasadena, California 91125.

References

- Glicken, H., and B. Voight, and R. J. Janda, Rockslide-debris avalanche of May 18, 1980, Mount St. Helens volcano, paper presented at the IAVCEI (International Association of Volcanology and Chemistry of the Earth's Interior) Symposium, Tokyo, Aug. 28 - Sept. 9, 1981.
- Kanamori, H., and J. W. Given, Analysis of long-period seismic waves excited by the May 18, 1980 eruption of Mount St. Helens - A terrestrial monopole?, J. Geophys. Res., 87, 5422-5432, 1982.
- Kanamori, H., and G. S. Stewart, A slow earthquake, Phys. Earth Planet. Int., 18, 167-175, 1979.
- Kanamori, H., and G. S. Stewart, Mode of the strain release along the Gibbs fracture zone, Mid-Atlantic Ridge, Phys. Earth. Planet. Inter., 11, 312-332, 1976.
- Kieffer, S. W., Blast dynamics at Mount St. Helens on 18 May 1980, Nature, 291, 568-570, 1981a.
- Kieffer, S. W., The lateral blast of May 18 at Mount St. Helens, paper presented at the IAVCEI (International Association of Volcanology and Chemistry of the Earth's Interior) Symposium, Tokyo, Aug. 28 - Sept. 9, 1981b.
- Malone, S. D., E. Endo, C. S. Weaver, and J. W. Ramey, Seismic monitoring for eruption prediction, The 1980 Eruptions of Mt. St. Helens, U.S. Geol. Surv. Prof. Pap., 1250, 803-813, 1982.
- Moore, J. G., The pyroclastic surge of May 18, 1980, Mt. St. Helens, Washington, paper presented at the IAVCEI (International Association of Volcanology and Chemistry of the Earth's Interior)

Symposium, Tokyo, Aug. 28 - Sept. 9, 1981.

Moore, J. G., and W. C. Albee, Topographic and structural changes, March-July 1980 - Photogrammetric data, The 1980 eruption of Mt. St. Helens, U.S. Geol. Surv. Prof. Pap., 1250, 123-141, 1981.

Moore, J. G., and C. J. Rice, Chronology and character of Mt. St. Helens explosive eruptive phase of May 18, 1980, preprint to be published in Explosive Volcanism, 1982.

Richards, P. G., Elementary solutions to Lamb's problem for a point source and their relevance to three-dimensional studies of spontaneous crack propagation, Bull. Seismol. Soc. Am., 69, 947-956, 1979.

Voight, B., H. Glicken, R. J. Janda, and P. M. Douglass, Catastrophic rockslide-avalanche of May 18, The 1980 Eruptions of Mount St. Helens, U.S. Geol. Surv. Prof. Pap., 1250, 347-378.

Weaver, Craig S., W. C. Grant, S. D. Malone and E. T. Endo, Post-May 18 seismicity: Volcanic and tectonic implications, The 1980 eruptions of Mt. St. Helens, U.S. Geol. Surv. Prof. Pap., 1250, 109-121, 1979.

Figure Captions

- Figure 1. P waves (vertical component) and S waves (transverse component) excited by the Mt. St. Helens eruption and recorded at the GDSN stations. The P and S waves are lined up with respect to the computed Jeffreys-Bullen P and S arrival times respectively. The stations with and without asterisks indicate ASRO and SRO stations respectively. The waveforms at ASRO stations should be shifted to the left by 4 sec for comparison with those at SRO stations. The numbers just below the station names indicate the peak-to-peak amplitude in digital counts. The distance and azimuth of each station are shown on the left. Note the same polarity of P waves at all the stations.
- Figure 2. The variation of the amplitudes as a function of azimuth. The amplitudes are equalized to that of an SRO station at a distance of 76° . Calculated amplitudes for a single force with dip angles $\delta = 0^{\circ}$ and $\delta = 60^{\circ}$ are indicated by solid (positive) and dotted (negative) curves. f is the magnitude of the force.
- Figure 3. The coordinate system used in this paper, the geometry of the force and the location of the station.
- Figure 4. a) Comparison of P and S waves observed at station GRF. Note the difference in the period. b) Top: Synthetic P-wave seismograms computed for a single force with a triangular

time history: t_w is the total width of the triangle, and $t_\alpha^* = 1$ sec. Middle: Synthetic S wave computed for the same source with $t_\beta^* = 4$ sec. Bottom: Synthetic S wave computed for a single force with $t_w = 35$ sec. For the computation of synthetic seismograms, the dip angle is arbitrarily assumed to be 60° to the south. Note the almost identical width of P and S waves computed for the same source ($t_w = 20$ sec). A triangular source with $t_w = 35$ sec can explain the period of the observed S wave.

Figure 5. Filtered SH wave: Note the polarity reversal between station ZOB and MAJ. The width of the filter function is indicated in the figure.

Figure 6. The azimuthal variation of the amplitude of the filtered SH wave. The amplitude computed for a horizontal single force determined from long-period surface waves is shown by solid and dotted curves.

Figure 7. Comparison of observed and synthetic waveforms of the filtered SH wave. The amplitudes are normalized. The synthetics are computed for a horizontal single force determined from long-period surface waves.

Figure 8. Comparison of observed and synthetic P waves for stations GRF and MAJ. The synthetics are computed for a vertical single force with the time history shown at the bottom. f_v is the peak value of the force.

Figure 9. P-wave first motions at stations LON and COR. For LON, the records from long-period (LP), intermediate-period (IP) and

short-period (SP) channels are shown, and the origin time of the $M_B = 5.2$ earthquake and the expected arrival time of the P wave are shown. For COR, the vertical component of the WWSSN long-period seismogram is shown, and the expected P time is indicated. Note the upward motion at this time. Geometrical relation of stations LON and COR with respect to Mt. St. Helens is also shown.

Figure 10. a) Intermediate-period seismogram observed at station LON ($\Delta = 68$ km, $\phi = 26^\circ$). b) The displacement time history obtained from a) by deconvolving the instrument response over a pass-band from 1.8 to 150 sec. c) WWSSN long-period seismograph response obtained by convolving b) with the instrument response. d) Displacement time history obtained from b) by using the dotted curve as the base line. e) Displacement time history obtained from b) by using the dash-dot curve as the base line.

Figure 11. Comparison of the seismograms recorded at stations LON (trace a) and GRF (trace b). Traces a and b are lined up with respect to the computed P time. Trace c is obtained from trace a by changing the polarity and shifting to the left by 9 sec. Note the better waveform match between traces b and c than a and b.

Figure 12. Comparison of the WWSSN-LP response at LON (trace c in Figure 10 and synthetic seismograms computed for the displacement time sequences S_1 (trace d in Figure 10) and S_2 (trace e in Figure 10).

Figure 13. Sequence of various events associated with the Mt. St. Helens eruption and the time history of the long-period horizontal single force and the short-period vertical force. References for the various events are Voight et al., (1982), Glicken et al., (1981), Moore (1981), Moore and Rice (1981), Malone et al (1982), and Kieffer (1981a,b).

ORIGINAL PAGE IS
OF POOR QUALITY

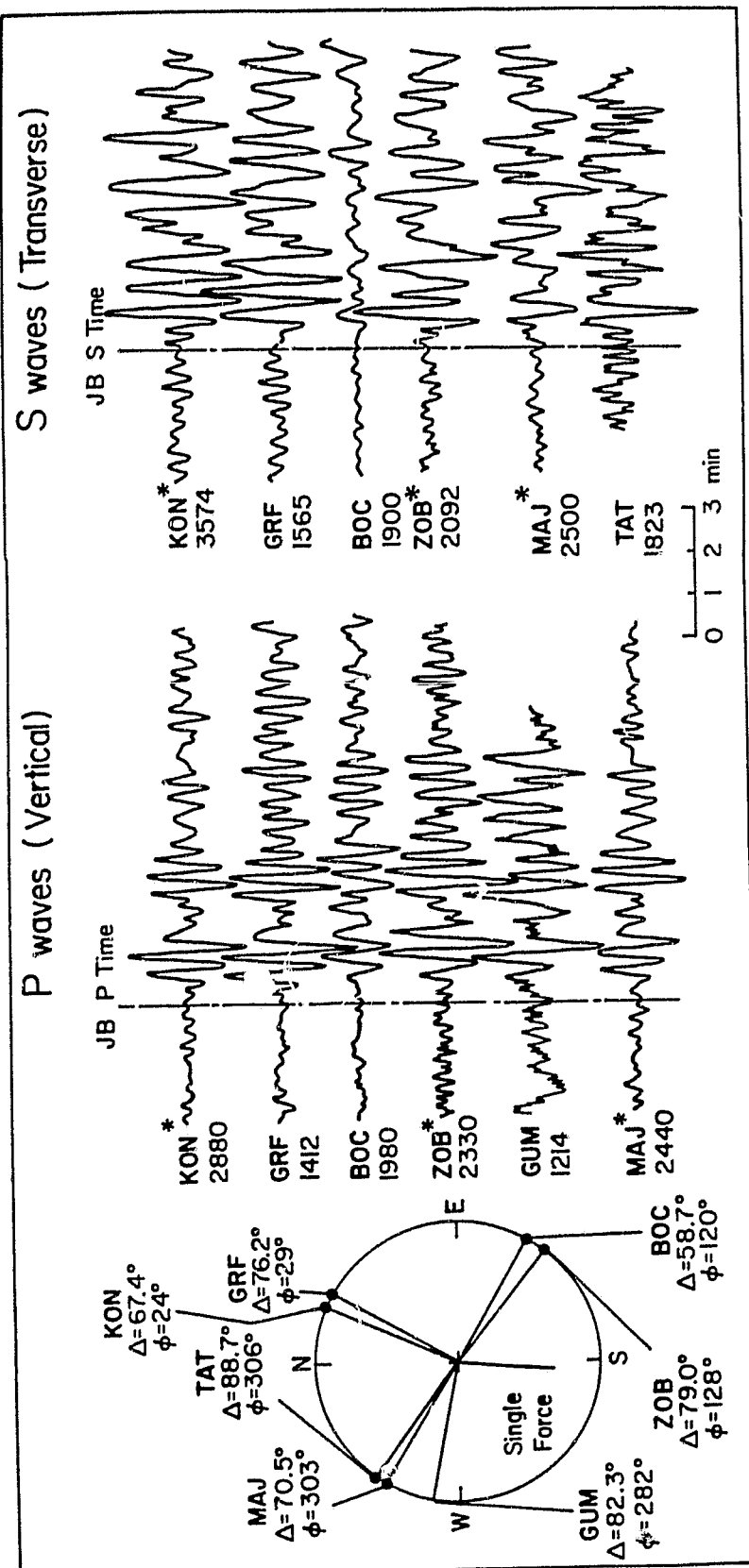


Fig. 1

ORIGINAL PAGE IS
OF POOR QUALITY

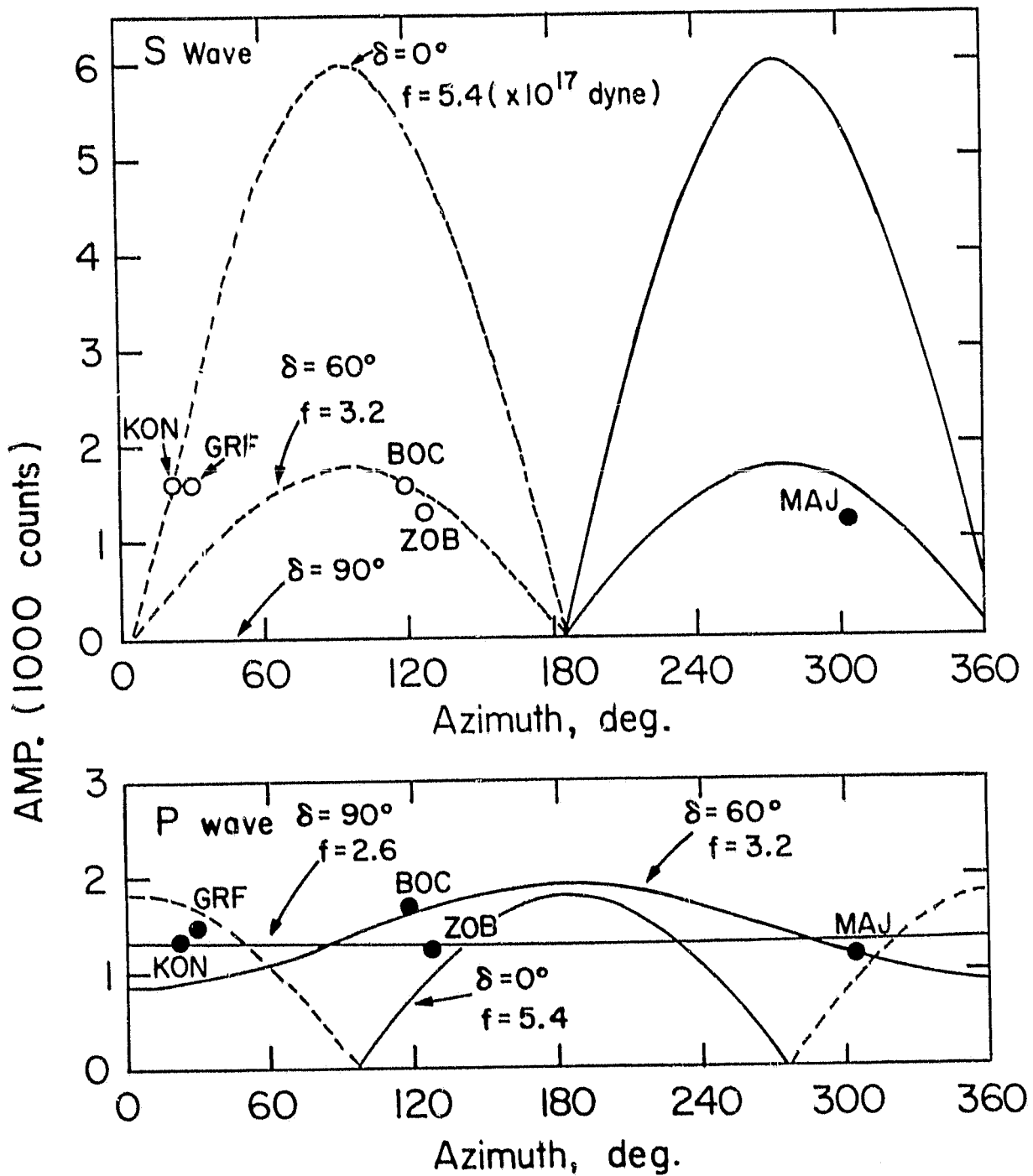


Fig. 2

ORIGINAL PAGE IS
OF POOR QUALITY

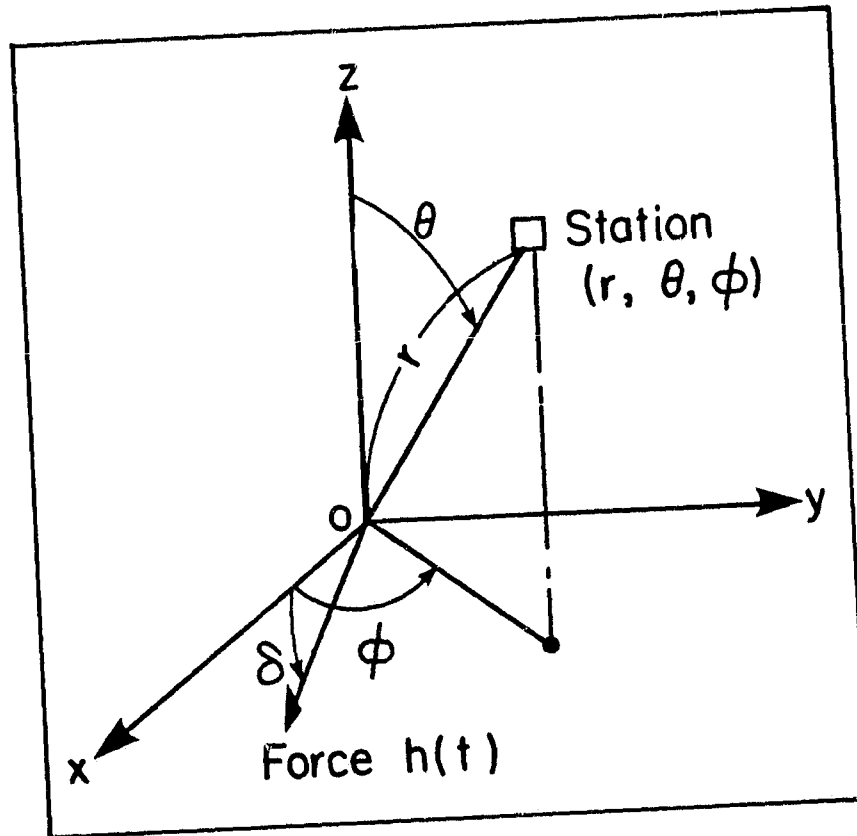
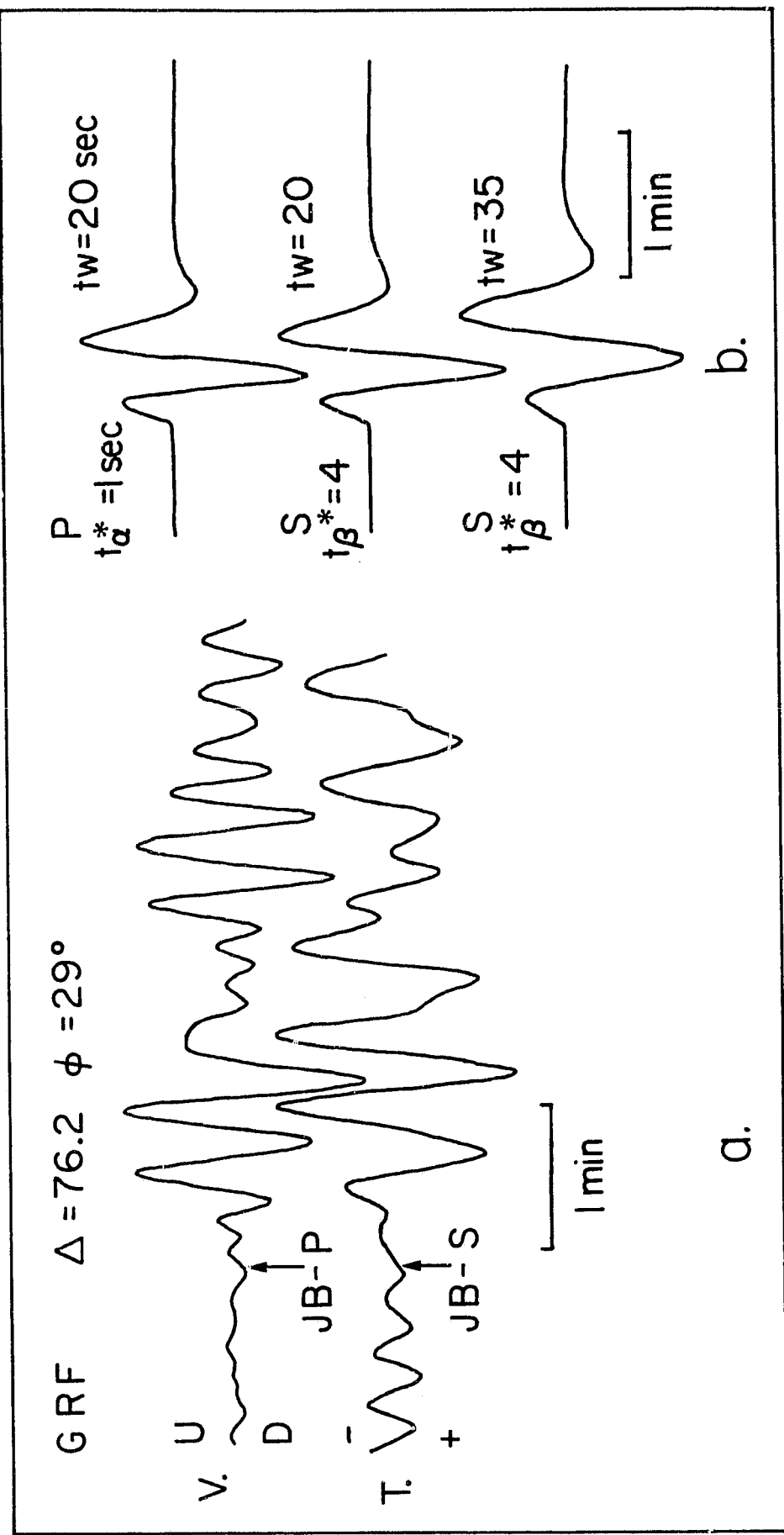


Fig. 3



ORIGINAL PAGE IS
OF POOR QUALITY

Fig. 4

ORIGINAL PAGE IS
OF POOR QUALITY

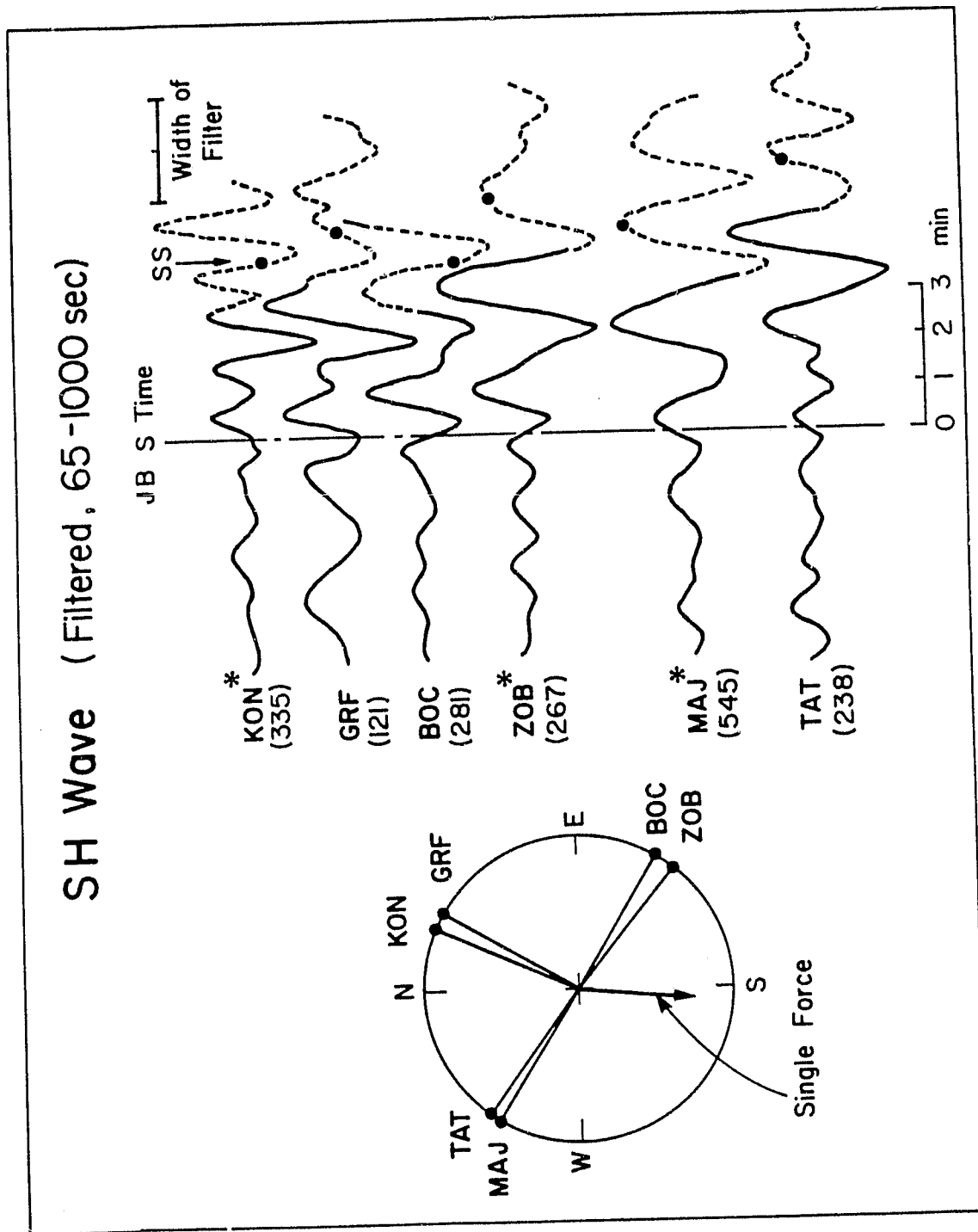


Fig. 5

ORIGINAL PAGE IS
OF POOR QUALITY

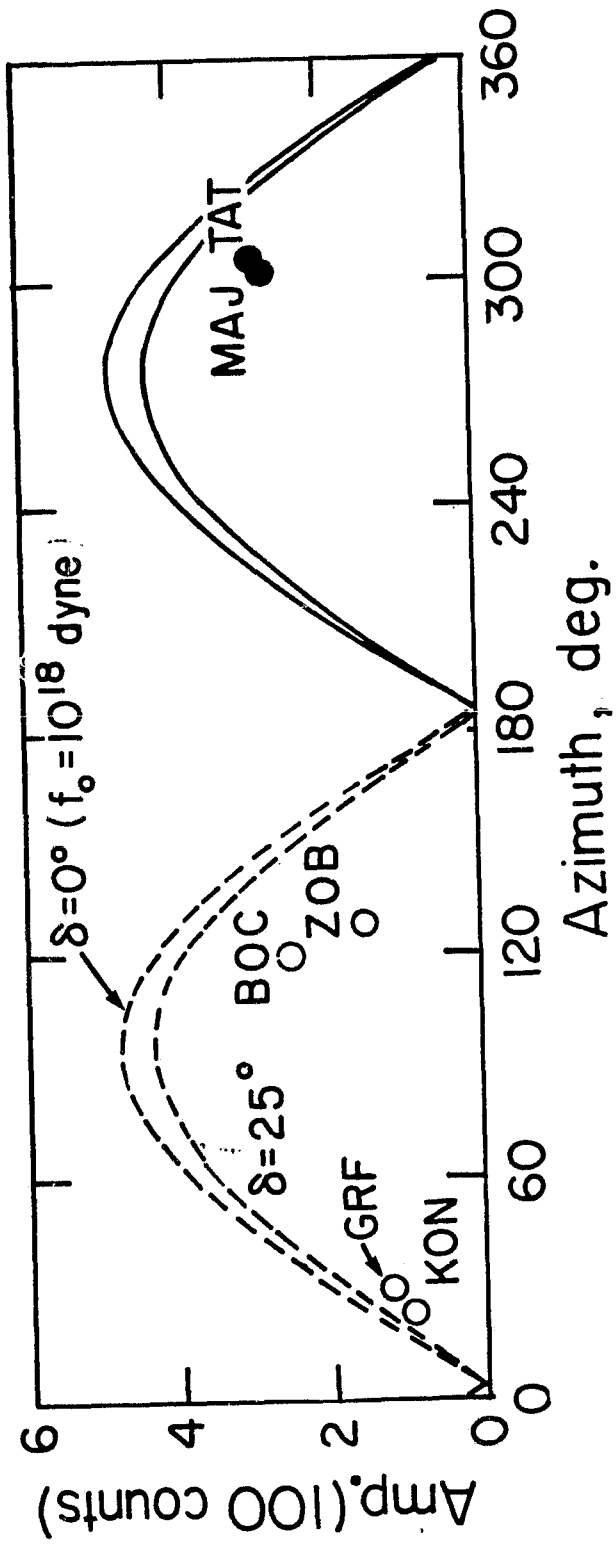


Fig. 6

ORIGINAL PAGE IS
OF POOR QUALITY

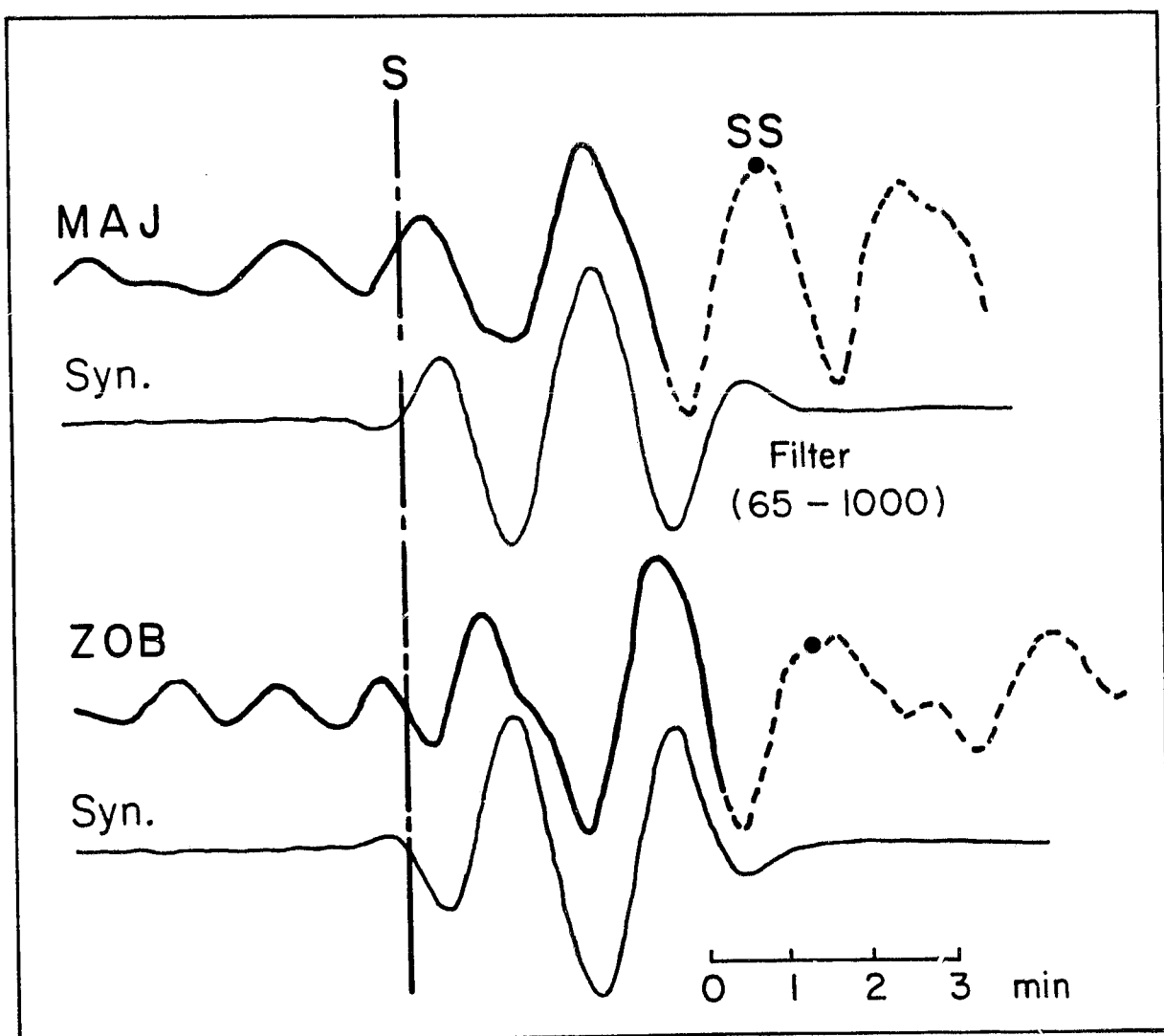


Fig. 7

ORIGINAL PAGE IS
OF POOR QUALITY

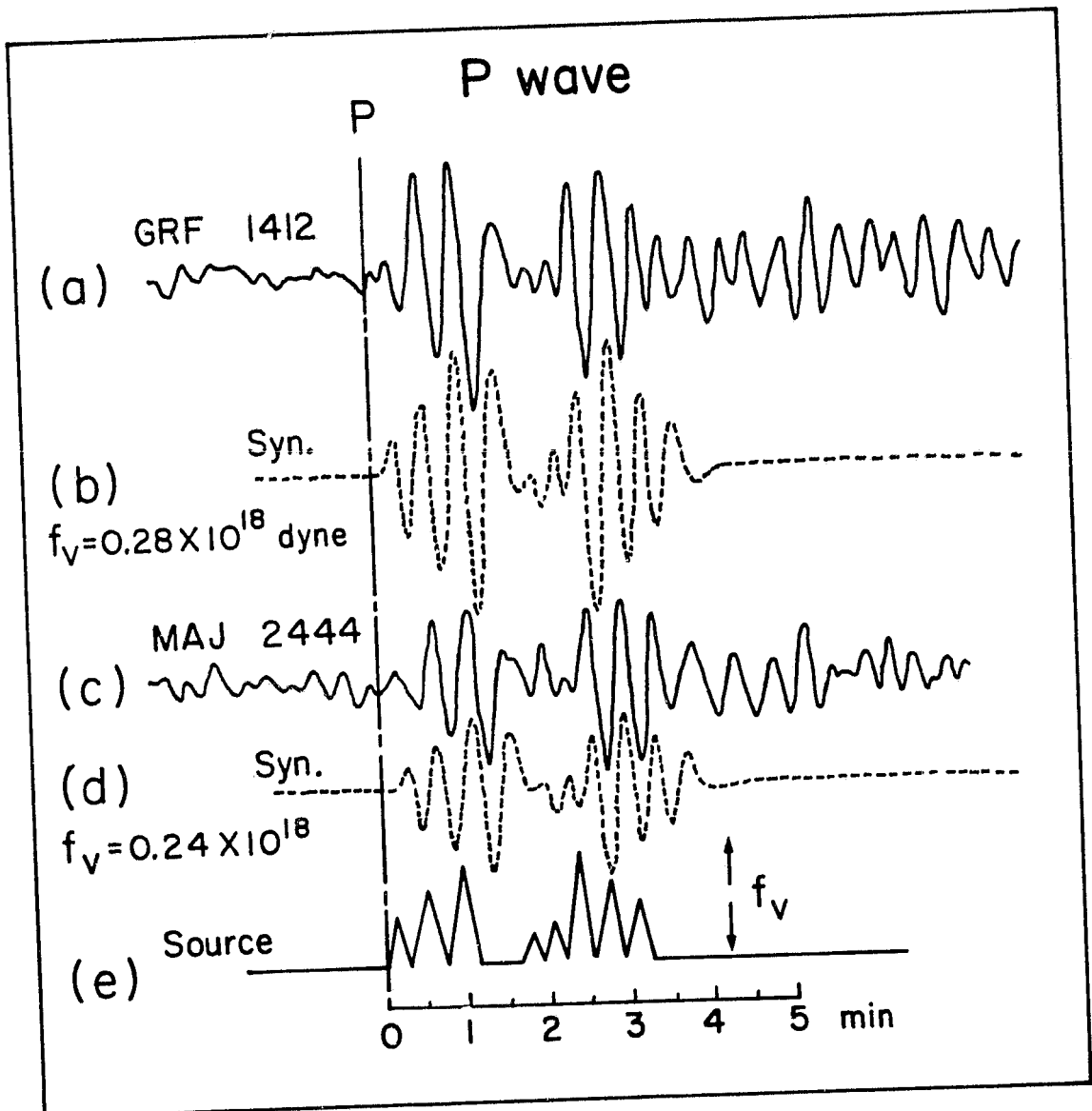
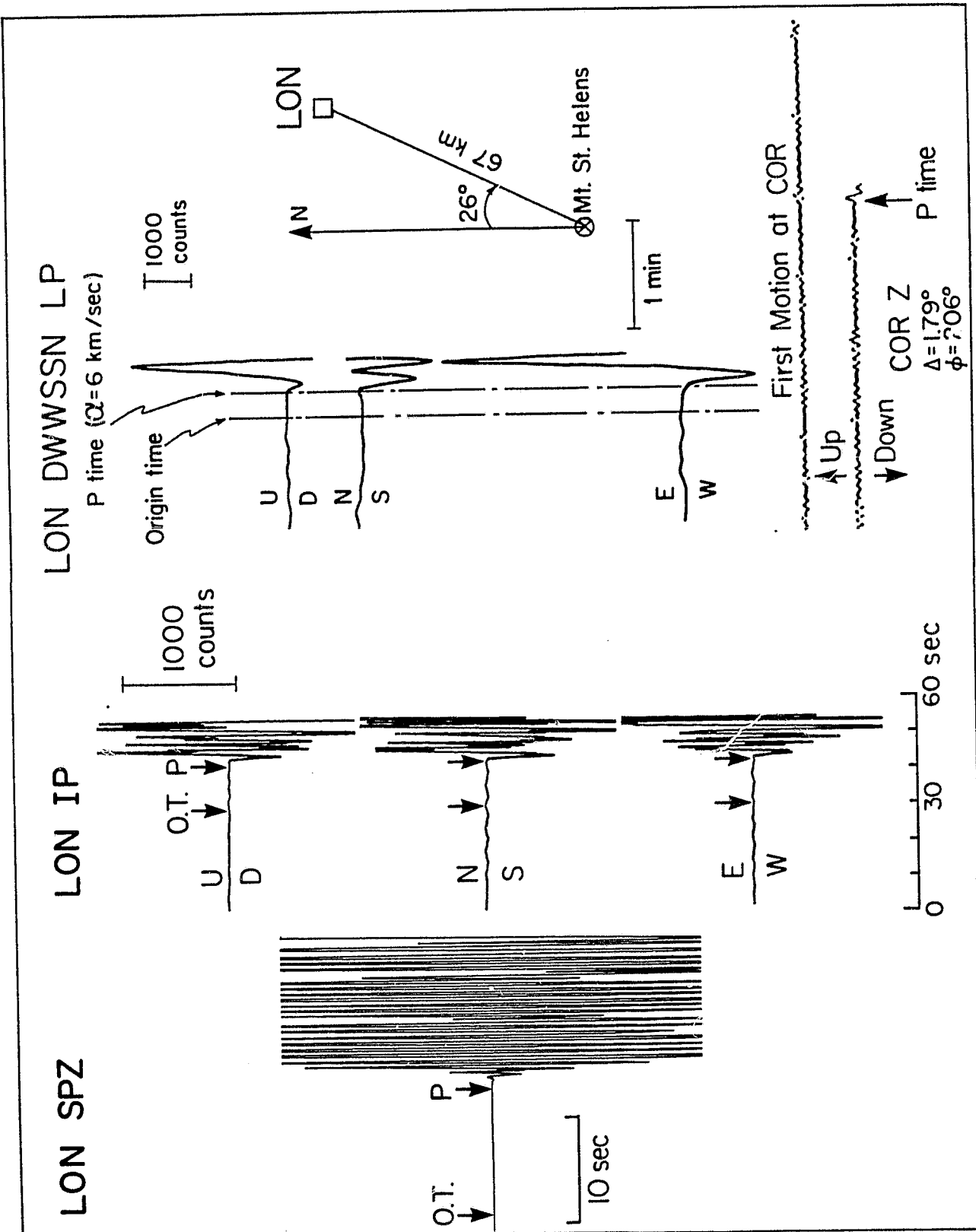


Fig. 8

ORIGINAL PAGE IS
OF POOR QUALITY

Fig. 9



ORIGINAL PAGE IS
OF POOR QUALITY

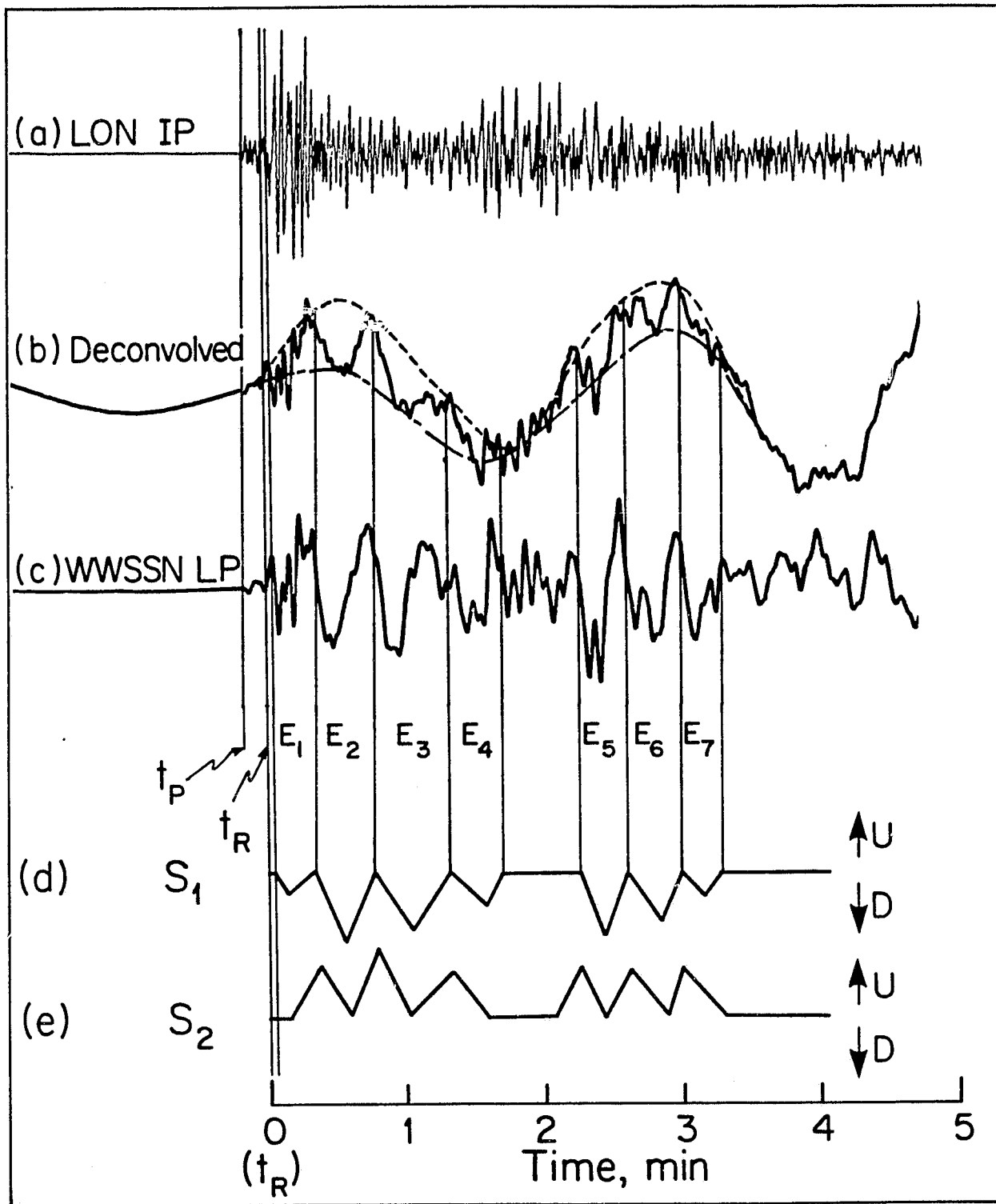


Fig. 10

ORIGINAL PAGE IS
OF POOR QUALITY

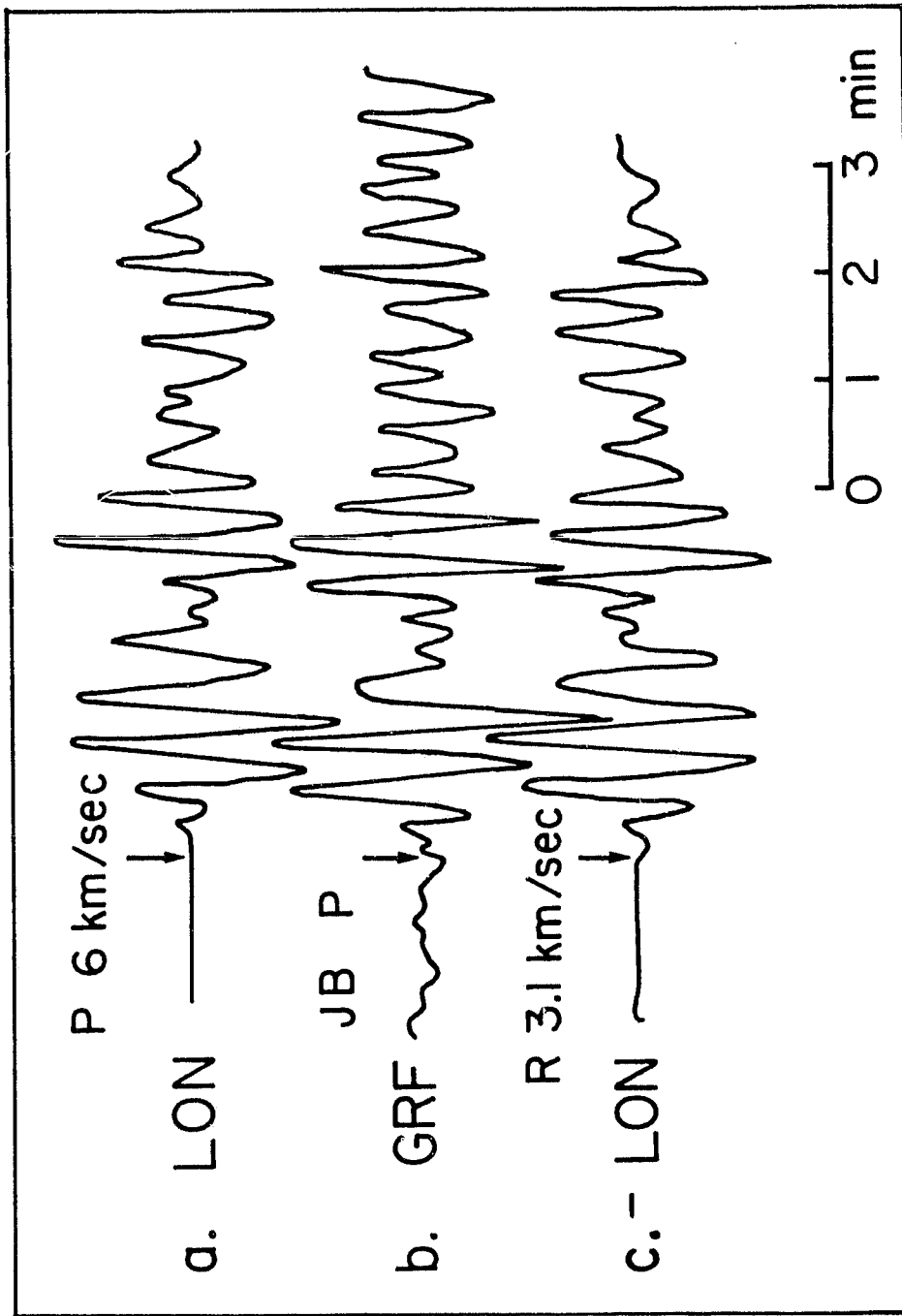


Fig. 11

ORIGINAL PAGE IS
OF POOR QUALITY

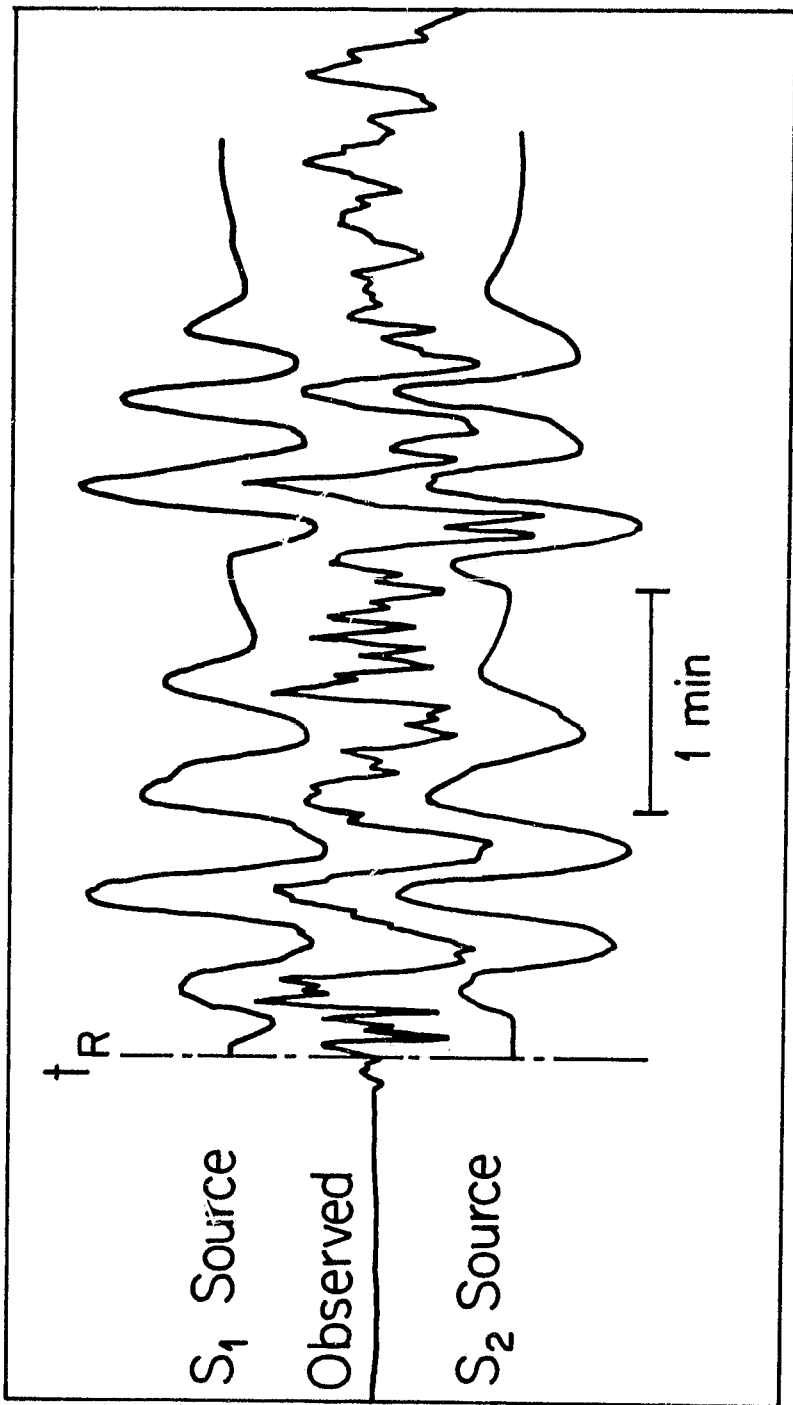


Fig. 12

ORIGINAL PAGE IS
OF POOR QUALITY

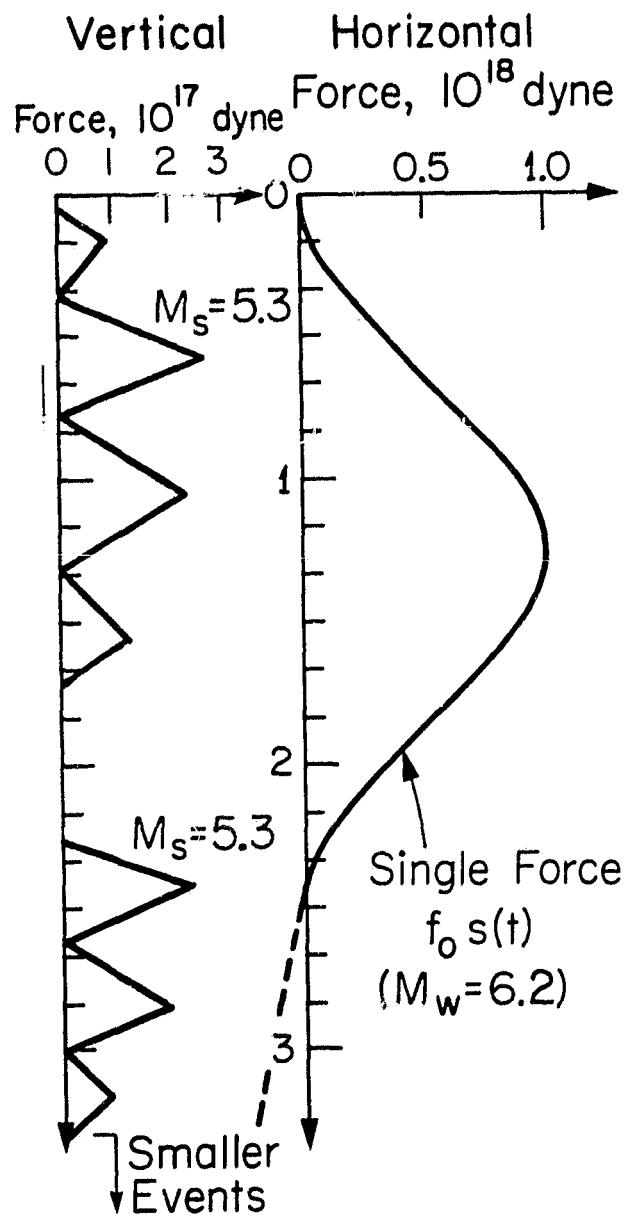
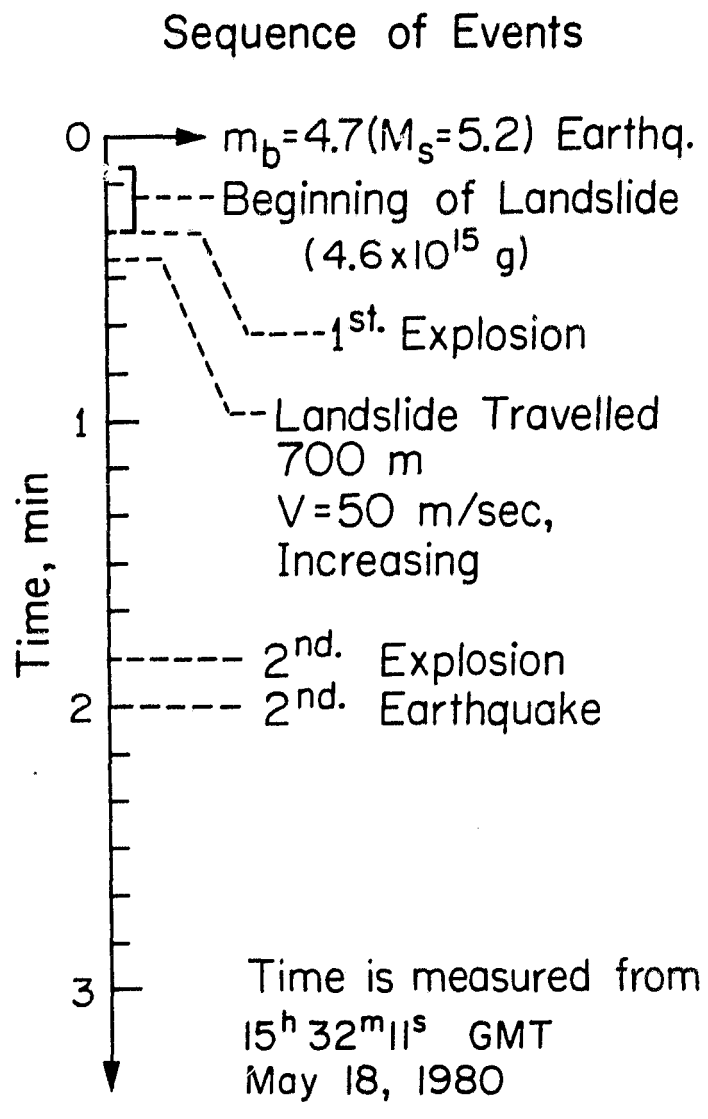


Fig. 13